Available online at www.sciencedirect.com
SCIENCE DIRECT®
International Journal of Solids and Structures 42 (2005) 1287–1307
INTERNATIONAL JOURNAL OF SOLIDS and STRUCTURES
www.elsevier.com/locate/ijsolstr

Anticlastic curvature in draw-bend springback

J.F. Wang [a], R.H. Wagoner [a,*], D.K. Matlock [b], F. Barlat [c]

[a] *Department of Materials Science and Engineering, The Ohio State University, 2041 College Road, Columbus, OH 43210, USA*
[b] *Department of Metallurgical and Materials Engineering, Colorado School of Mines, Golden, CO 80401, USA*
[c] *Materials Science Division, Alcoa Technical Center, 100 Technical Drive, Alcoa Center, PA 15069, USA*

Received 2 August 2004; received in revised form 17 August 2004
Available online 2 November 2004

Abstract

Draw-bend springback shows a sudden decline as the applied sheet tension approaches the force to yield the strip. This phenomenon coincides with the appearance of *persistent anticlastic curvature*, which develops during the forming operation and is maintained during unloading under certain test conditions. In order to understand the mechanics of persistent anticlastic curvature and its dependence on forming conditions, aluminum sheet strips of widths ranging from 12 to 50 mm were draw-bend tested with various sheet tensions and tool radii. Finite element simulations were also carried out, and the simulated and measured springback angle and anticlastic curvature were compared. Analytical methods based on large deformation bending theory for elastic plates were employed to understand the occurrence and persistence of the anticlastic curvature. The results showed that the final shape of a specimen cross-section is determined by a dimensionless parameter, which is a function of sheet width, thickness and radius of the primary curvature in the curled region of an unloaded sample. When the normalized sheet tension approaches 1, this parameter rapidly decreases, and significant anticlastic deflection is retained after unloading. The retained anticlastic curvature greatly increases the moment of inertia for bending, and thus reduces springback angle.
© 2004 Elsevier Ltd. All rights reserved.

Keywords: Aluminum; Anticlastic; Bending; Plate; Springback

1. Introduction

When a long, flat rectangular sheet of uniform thickness is bent about an axis parallel to one of its edges, say in the x-direction, a transverse curvature is developed in the direction parallel to the bending axis (Lamb, 1891). For elastic deformation, this happens by the differential lateral contraction caused by

* Corresponding author. Tel.: +1 614 292 2079; fax: +1 614 292 6530.
E-mail address: wagoner.2@osu.edu (R.H. Wagoner).

0020-7683/$ - see front matter © 2004 Elsevier Ltd. All rights reserved.
doi:10.1016/j.ijsolstr.2004.08.017

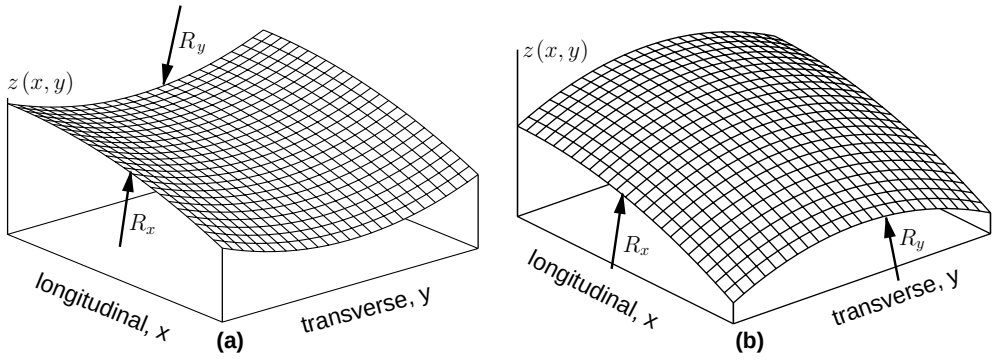

Fig. 1. Distorted plate surface after bending: (a) anticlastic and (b) synclastic.

Poisson's effect. Consequently, the initially flat surface becomes an *anticlastic surface*, with two orthogonal curvatures of opposite sign, Fig. 1(a). If the centers of these two curvatures appear on the same side of the surface, the surface is *synclastic*, Fig. 1(b). For narrow, initially flat sheets, the ratio between the longitudinal (i.e., primary, x-direction) and the transverse (i.e., secondary, y-direction) curvatures is given by the Poisson's ratio v, i.e., $R_y = vR_x$ (Yu and Zhang, 1996).

The shape of the cross-section of a bent beam or plate depends on a dimensionless parameter, $\beta = \frac{W^2}{R_x t}$, with W, t and R_x being the sheet width, thickness and radius of the primary bending curvature, respectively (Searle, 1908). The anticlastic surface has a constant curvature of $-\frac{v}{R_x}$, when β is less than unity (Ashwell, 1950). In this case, the sheet behaves like a plane-stress beam. However, if β is larger than 20, the anticlastic deflection is mainly confined to the sheet edges, while the sheet central area stays relatively flat (Ashwell and Greenwood, 1950a,b; Bellow et al., 1965). Consequently, the deformation state can be characterized as more *plate-like*, with plane-strain the limiting approximation. The deformation modes may be interpreted in terms of "body force" which tends to suppress the formation of a large circular cross-section (Horrocks and Johnson, 1967). When bending wide sheets to a small radius, the constrained anticlastic curvature causes a biaxial stress state on the tension side of the sheet (Gerard, 1946).

The principles of simple elastic plate bending have been extended to bodies of varying thickness (Fung and Wittrick, 1954; Conway and Nickola, 1965; Conway and Farnham, 1965; Pao and Conway, 1966), to anisotropic single crystal silicon (Kaldor and Noyan, 2002a,b), and to specimens plastically deformed in four-point bending tests (Horrocks and Johnson, 1967). In the last case, pertinent to the current work, it was concluded that plasticity affected the magnitude of the anticlastic curvature, but had little effect on springback.

There is little literature on anticlastic deflection for more complicated forming processes. Anticlastic displacements up to 1.5 times the sheet thickness have been measured after draw-bending and unloading (Carden et al., 2002; Li et al., 2002), in marked contrast to simple bending results where theory predicts a maximum deflection of about 10% of the sheet thickness. For small sheet tensions, the anticlastic curvature developed during forming nearly disappeared during unloading, thus having little effect on final specimen shape (consistent with observations for springback in simple bending). However, as sheet tension was increased to the yield stress of the material, the anticlastic distortion persisted after unloading. This *persistent anticlastic distortion* increased the moment of inertia of the specimen greatly, and thus reduced springback commensurately (Carden et al., 2002).

This investigation focuses on the role of anticlastic curvature in springback following draw-bend deformation. The mechanics of persistent anticlastic curvature is sought, especially its dependence on forming parameters and specimen geometry. In order to proceed, the classic theory of bending elastic plate is

reviewed. Draw-bend test results are then presented, and they are considered with the aid of the theory and finite element simulations. Discussions and conclusions are then drawn.

2. Draw-bend experiment

The draw-bend test can closely mimic industrial forming processes, where sequential bending and unbending takes place under superimposed tension as sheet material is drawn over a rigid tool surface (Carden et al., 2002). Unlike other laboratory (and industrial) forming tests, where stretching is usually provided through various locking mechanisms (draw-bead or blank holder), sheet tension can be directly and precisely controlled in the draw-bend test, using a secondary hydraulic cylinder which is programmed to provide constant stretching force during the test (Vallance and Matlock, 1992). In this study, 6022-T4 aluminum strips were tested using a special draw-bend machine at Colorado School of Mines. Details of this equipment and procedures can be found elsewhere (Wenzloff et al., 1992; Carden et al., 2002).

Rectangular specimens were sheared with their lengths parallel to the sheet rolling direction. As shown in Fig. 2, the draw-bend test procedure consists of three steps. The first step involves bending the flat sheet to conform to the tool, with 90° of contact. A prescribed back force is next applied to the left end of the strip, and the strip is drawn over an unrotating tool by imposing a constant speed of 40 mm/s to the right end of the strip, while the back force is kept constant. F_b (the normalized back force) is expressed as the back force divided by the yielding force of the specimen in uniaxial tension. Standard industrial lubricant (Parco Prelube MP 404, 2001) was brushed on both the strip and tool surfaces to provide medium friction (Carden et al., 2002). After the drawing distance reaches 127 mm, the final step involves unloading of the specimen, removal from the grips, and measurement. The specimen shapes were traced on paper and then recorded digitally. Traces were first taken one minute after forming and unloading, then repeated at intervals up to 15 months for time-dependent springback measurement (Wang et al., 2004). The current work only studies the static springback, that is, as measured approximately one minute after unloading.

A typical unloaded specimen is depicted in Fig. 2, with four deformation regions delineated. *Regions 1* and *4* remain straight throughout the test. *Region 2* was in contact with the forming tool just before unloading, and its radius of curvature changes from R to R' after springback. The important specimen geometry is

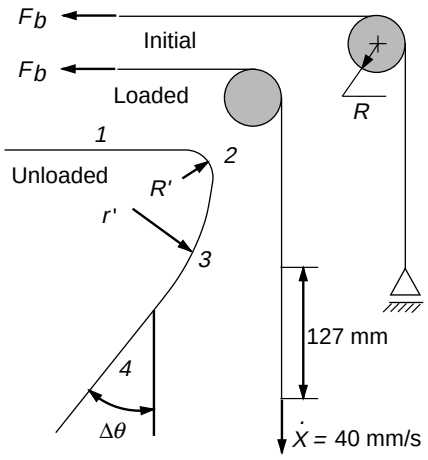

Fig. 2. Schematic of the stages of the draw-bend test and unloaded specimen geometry.

defined by *Region 3*, which has a radius of curvature r' after unloading. It is a measure of the so-called "sidewall curl" that is observed in many sheet-formed parts (Davies, 1984). Springback may be characterized by the springback angle $\Delta\theta$, Fig. 2.

A transverse curvature in the sheet width direction was discovered in some draw-bend tested strips (Carden et al., 2002). If the transverse cross-section is assumed to be circular, the radius of this anticlastic curvature, R_a, can be calculated according to

$$R_a = \frac{\Delta h}{2} + \frac{W^2}{8\Delta h} \tag{1}$$

where Δh is the arc height of the cross-section (Carden et al., 2002). Δh was measured at the center point of *Region 3* (Fig. 2) of an unloaded specimen, using a digital caliper with 0.01 mm resolution. The complete cross-section profile was measured by a 0.03 mm resolution dial gauge for two draw-bend tested samples. The anticlastic deflection for other specimens was measured at the center only. The measured Δh varies from 0.1 to 1.6 mm (i.e., $R_a = 200$–3600 mm). The specimen-to-specimen (under same test conditions) scatter of R_a is 10–90 mm.

3. Finite element modeling

Simple bending of initially flat and curved elastic plates was simulated by finite element (FE) modelings, and results were compared with the closed-form solution (as will be discussed in the next section). 4-Node shell elements with reduced integration (type S4R) were used (Abaqus, 2001), with 15 integration points through the sheet thickness ($t = 1$). The elastic modulus and Poisson's ratio adopted in simulations were 65 GPa and $\frac{1}{3}$, respectively. Mirror symmetry was utilized and only one quarter of the plate was modeled, with symmetric boundary conditions applied at the plate edges. Pure bending was attained by applying prescribed rotations to edge nodes.

The static springback in the draw-bend test was simulated, for a range of back force ($0.1 \leqslant F_b \leqslant 1.2$), specimen width ($W = 12$–$50$ mm) and tool radius (3.2–12.7 mm). Both 2D and 3D analysis were carried out, using plane-stress beam element (Abaqus type B21), and 4-node shell element with reduced integration (S4R), respectively (Abaqus, 2001). The sheet strip was modeled by 300 elements of non-uniform size in the longitudinal direction. Smaller elements were used in the contact areas (*Regions 2* and *3*, Fig. 2) to ensure numerical accuracy, with one contact node per 4.5° of turn angle (Li et al., 2002). In 3D FE models, only half of the physical strip was modeled because of the mirror symmetry, with 8 elements in the sheet-width direction. Fifty-one integration points were used through the sheet thickness, for both B21 and S4R elements, to minimize numerical error (Li et al., 2002). In order to closely represent plastic anisotropy of 6022-T4 sheet, the Barlat'96 yield function (Barlat et al., 1997) and a modified anisotropic hardening model were adopted. A friction coefficient of 0.15 was used for lubricated test conditions. These choices of material and friction parameters have been shown to closely reproduce the observed springback behavior for this alloy (Geng and Wagoner, 2002; Carden et al., 2002).

Simple bending theory suggests that the draw-bend process using standard specimens ($W/t = 55$) is closer to plane-strain deformation (Marciniak and Duncan, 1992). However, 2D finite element simulations demonstrated that plane-stress (with B21 beam element) results were consistently better than plane-strain (with S4R shell element) (Li et al., 2002). In the FE models, the plane-strain assumption was enforced by prescribing zero lateral displacement to all nodes in the width direction. For the sake of simplicity, von Mises yield function and isotropic hardening law were used in these simulations. As shown in Fig. 3, simulations using 2D beam elements are in better agreement with experimental data than that of plane-strain, Fig. 3(a). It is also noted that 2D simulations introduce significant error for larger back forces, because neither plane-stress nor plane-strain reproduces the anticlastic curvature. Full 3D simulations correctly

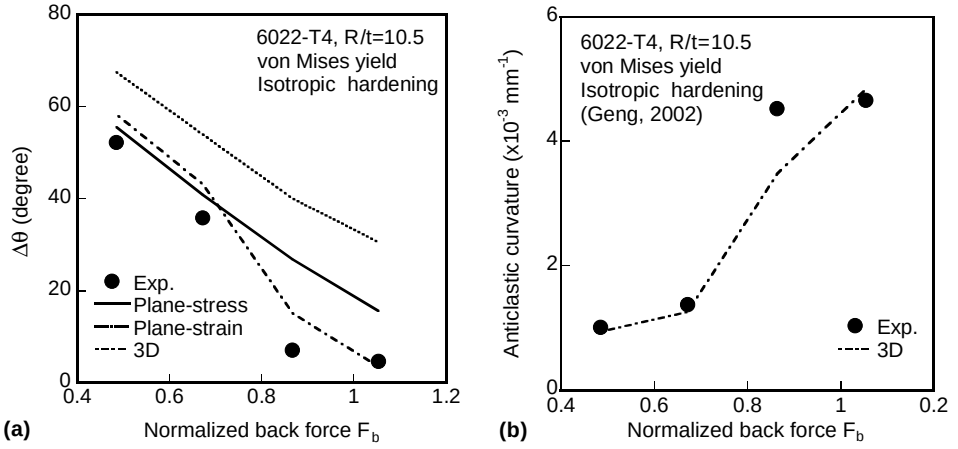

Fig. 3. Simulated springback angle using various assumptions.

reproduce the fast decline of springback angle as F_b approaches 0.7–0.8. This phenomenon is correlated to the appearance of *persistent anticlastic curvature*, Fig. 3(b), which will be explored in detail.

4. Elastic theory for plate bending

Before interpreting the anticlastic curvature during and after draw-bending, the simpler case of pure bending is considered. The classic bending theory of elastic plate is summarized here, while details can be found elsewhere (Ashwell, 1950, 1952). The results are based on the work of Ashwell (1950, 1952), which makes use of Marguerre's large deformation theory of plate bending (Marguerre, 1938) and extends von Kármán's analysis (von Kármán, 1910). Unlike small deformation theory, the membrane stress at the plate's middle surface is considered.

The general theory is first introduced, with approximations suitable for closed-form solution. Then, these results are applied to two cases of interest for the draw-bend application: (1) bending of an initially flat sheet, and (2) unbending (straightening) of a curved sheet. These two operations are investigated because they correspond to the bending and unbending experienced by the cross-sections of the draw-bend specimen as they are drawn sequentially over the tool radius.

4.1. Closed-form solution

The problem of bending an initially curved plate is shown schematically in Fig. 4. A rectangular plate (dimension L, W and t), with initial middle surface shape described by $z_0(x,y)$ and radii of curvature R_{x0} and R_{y0}, is subjected to a bending moment m_x per unit width applied to the plate edges, i.e., at $x = \pm\frac{L}{2}$.

The problem may be solved in closed form with the simplifying assumptions that the initial and final mid-plane shapes are described parabolically by

$$z_0(x,y) = \frac{x^2}{2R_{x0}} + \tilde{z}_0(y) = \frac{x^2}{2R_{x0}} + \frac{y^2}{2R_{y0}} - \frac{W^2}{12R_{y0}} \tag{2}$$

$$z(x,y) = \frac{x^2}{2R_x} + \tilde{z}(y) \tag{3}$$

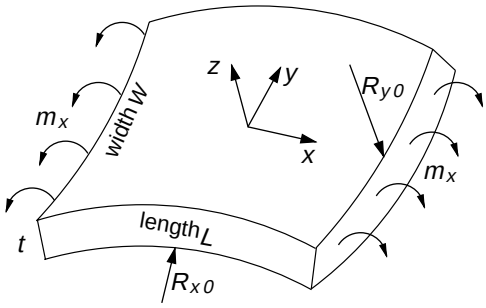

Fig. 4. Schematics of plate bending problem in the Cartesian coordinate system.

where R_x and R_y are the respective radii of curvature after deformation (Ashwell, 1952), and $\tilde{z}(y)$ is the final, arbitrary anticlastic shape that is sought. Under these conditions, the anticlastic profile $\tilde{z}(y)$ for an initially singly-curved plate ($\frac{1}{R_{x0}} = 0, \frac{1}{R_{y0}} \neq 0$) can be solved from the following fourth-order, homogeneous ordinary differential equation:

$$\frac{\mathrm{d}^4\tilde{z}}{\mathrm{d}y^4} + 4\gamma^4\tilde{z} = 0 \quad \text{with} \quad \gamma^4 = \frac{3(1-\nu^2)}{R_x^2 t^2} \tag{4}$$

The solution of the above ODE is (Ashwell, 1952)

$$\frac{\tilde{z}}{t} = \frac{\frac{R_x}{R_{y0}} - \nu}{\sqrt{3(1-\nu^2)}}(K_1 \cosh \gamma y \cos \gamma y + K_2 \sinh \gamma y \sin \gamma y) \tag{5}$$

where

$$K_1 = \frac{\sinh\left(\frac{\gamma W}{2}\right)\cos\left(\frac{\gamma W}{2}\right) - \cosh\left(\frac{\gamma W}{2}\right)\sin\left(\frac{\gamma W}{2}\right)}{\sinh \gamma W + \sin \gamma W}$$

$$K_2 = \frac{\sinh\left(\frac{\gamma W}{2}\right)\cos\left(\frac{\gamma W}{2}\right) + \cosh\left(\frac{\gamma W}{2}\right)\sin\left(\frac{\gamma W}{2}\right)}{\sinh \gamma W + \sin \gamma W}$$

For an initially doubly-curved plate ($\frac{1}{R_{x0}} \neq 0, \frac{1}{R_{y0}} \neq 0$), an approximate solution of the anticlastic profile is

$$\frac{\tilde{z}}{t} = \frac{\frac{R_x}{R_{y0}} + \frac{\nu R_x}{R_{x0}} - \nu}{\sqrt{3(1-\nu^2)}}(K_1 \cosh \gamma y \cos \gamma y + K_2 \sinh \gamma y \sin \gamma y) \tag{6}$$

4.2. Results for pure bending of an initially flat plate ($\frac{1}{R_{x0}} = \frac{1}{R_{x0}} = 0$)

Eq. (5) maybe used to visualize the anticlastic curvature for a range of plate widths and primary curvatures. Fig. 5 shows the variation of the normalized anticlastic deflection and the normalized transverse stress along the plate width direction, for a rectangular plate ($W = 50$ and $t = 1$) bent to various curvatures.

As shown in Fig. 5(a), the anticlastic displacement tends to localize toward the plate edges as β increases, while the plate center remains relatively flat. Correspondingly, more transverse stress is developed in the central area of the plate, but it decays to zero at the plate edges, Fig. 5(b). As β increases, the area with biaxial stress state expands, and the transverse stress drops faster near the edges. In the limit of $\beta = \infty$, the center of the plate approaches plane-strain, with $\sigma_{22} = \nu\sigma_{11}$, as illustrated by the thin dotted line in Fig. 5(b). From elastic plate theory, it is known that a lateral bending moment, $m_y = \nu m_x$, exists over

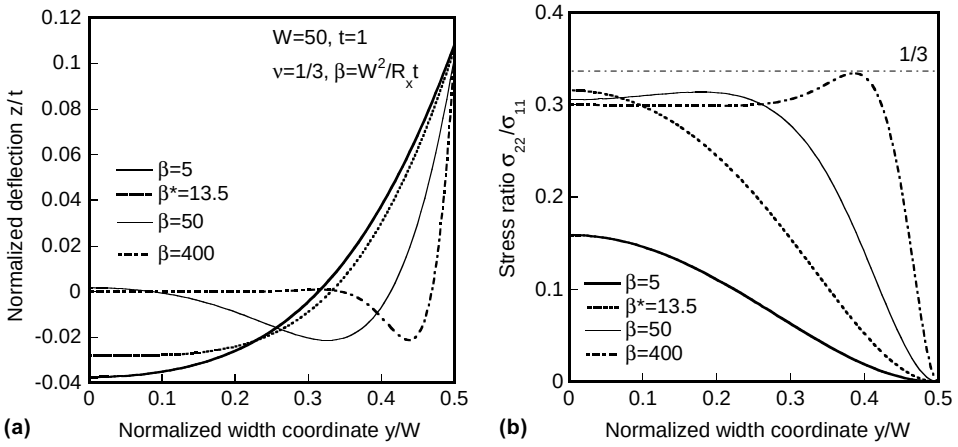

Fig. 5. Elastic solution of bending initially flat plate: (a) normalized anticlastic deflection and (b) stress ratio.

the flat portion of the deformed plate to maintain a cylindrical surface. However, m_y must equal zero at the edges. As pointed out by Fung and Wittrick (1955), the near-edge region with localized anticlastic deformation acts as a boundary layer through which the later bending moment is built up, from zero at the edge, to νm_x at the center.

The critical value, β^*, at which the anticlastic deflection curve starts to change its shape and first exhibits an inflection point, can be calculated by solving the following equation:

$$\left[\frac{\mathrm{d}^2\tilde{z}}{\mathrm{d}y^2}\right]_{y=0} = 0 \Rightarrow \tan\left(\frac{\gamma W}{2}\right) + \tanh\left(\frac{\gamma W}{2}\right) = 0 \tag{7}$$

where $\gamma W = \sqrt{\beta}\sqrt[4]{3(1-\nu^2)}$. The first root of the above transcendental equation is $\beta^* = 13.5$ for $\nu = \frac{1}{3}$.

The maximum anticlastic deflection, which occurs at plate edges, can be determined as follows. Knowing that $\sinh(\gamma W) \approx \cosh(\gamma W) \to \frac{1}{2}\mathrm{e}^{\gamma W}$ as $\gamma W \to \infty$, and the constants K_1 and K_2 in Eq. (5) become

$$K_{1,2} = \mathrm{e}^{-\gamma W/2}\left[\cos\left(\frac{\gamma W}{2}\right) \mp \sin\left(\frac{\gamma W}{2}\right)\right] \tag{8}$$

Near the plate edges, approximations are also made such that $\sinh(\gamma y) \approx \cosh(\gamma y) \to \frac{1}{2}\mathrm{e}^{\gamma y}$. Therefore, the normalized anticlastic deflection from Eq. (5) becomes

$$\frac{\tilde{z}}{t} = \frac{\left(\frac{R_x}{R_{y0}} + \frac{\nu R_x}{R_{x0}} - \nu\right)}{\sqrt{12(1-\nu^2)}}\left[\sin(\gamma\bar{y}) - \cos(\gamma\bar{y})\right] \tag{9}$$

where $\bar{y} = \frac{W}{2} - y$ is the distance measured from the plate edge toward the plate center. For an initially flat plate, i.e., $\frac{1}{R_{x0}} = \frac{1}{R_{y0}} = 0$, the maximum deflection occurs at the plate edges ($\bar{y} = 0$), and depends only on Poisson's ratio:

$$\left(\frac{\tilde{z}}{t}\right)_{\max} = \frac{\nu}{\sqrt{12(1-\nu^2)}}. \tag{10}$$

For $\nu = \frac{1}{3}$, the maximum anticlastic deflection $\tilde{z}_{\max}$ is about 10.2% of the sheet thickness.

In comparison with the closed-form solution, a series of elastic finite element simulations were conducted for pure bending of an initially flat sheet ($t = 1$) with various widths and bending radii, as listed in Table 1.

Table 1
Parameters used in the finite element model for elastic bending

β	Case	W (mm)	L (mm)	R (mm)	Mesh ($W \times L$)
5	a	5	8	5	10×32
	b	10	32	20	10×64
	c	20	128	80	10×128
100	a	25	10	6.25	25×20
	b	50	40	25	25×40
	c	100	160	100	25×80

The finite element meshes are so chosen that the element aspect ratio is 1. Further refinement showed negligible difference in results, as will be shown later. In order to assess the invariance of the result for fixed β, this parameter is rewritten in terms of non-dimensional quantities as follows:

$$\beta = \frac{W^2}{Rt} = \frac{(W/t)^2}{(R/t)} \tag{11}$$

The second form reveals the relationship of β to thickness-normalized specimen width (W/t) and bending radius (R/t).

The simulation results for $\beta = 5$ are compared with analytic solutions in Fig. 6, using three combinations of strip widths and bending radii. The simulated anticlastic profiles agree well with the closed-form solutions for this intermediate case (that is, it is intermediate between the plane-stress and plane-strain limits). As justified by one case ($W = 20$ mm), 15 through-thickness integration points are sufficient for elastic simple bending simulation.

For larger β, the analytic solution predicts that the anticlastic deflection is more concentrated toward the sheet edges. This is confirmed by finite element results for $\beta = 100$, as shown in Fig. 7(a). The stress state in the sheet center area is close to plane-strain, with stress ratio $\frac{\sigma_{22}}{\sigma_{11}}$ approaching Poisson's constant, see Fig. 7(b). Mesh refinement shows negligible difference in displacement and stress solution, as illustrated by the selected case for $W = 50$ mm, Fig. 7.

Conventional wisdom usually distinguishes plane-stress bending from plane-strain bending by the ratio of width to thickness (Marciniak and Duncan, 1992). For example, plane-stress bending is assumed

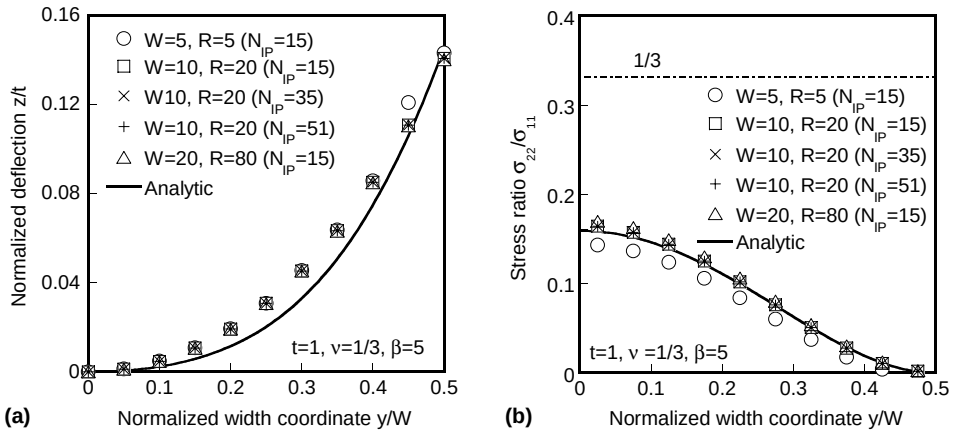

Fig. 6. FEM validation of the elastic solution for $\beta = 5$: (a) normalized anticlastic deflection and (b) stress ratio.

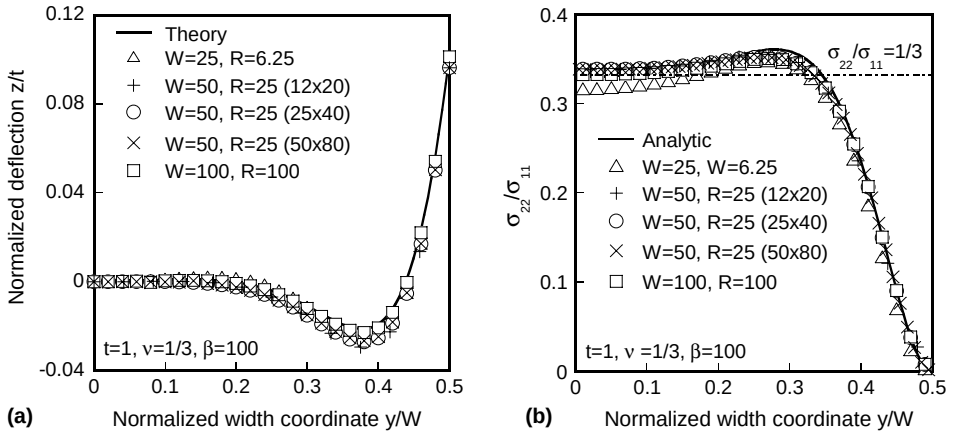

Fig. 7. FEM validation of the elastic solution for $\beta = 100$: (a) normalized anticlastic deflection and (b) stress ratio.

for $W/t \ll 1$ and plane-strain for $W/t \gg 1$. For these two limiting cases, the primary curvature is proportional to the bending moment M, according to elementary bending theory:

$$\frac{1}{R_x} = \begin{cases} \frac{M}{EI}, & \text{plane-stress} \\ \dfrac{M(1-\nu^2)}{EI}, & \text{plane-strain} \end{cases} \tag{12}$$

where I is the section moment of inertia. Based on the previous analysis, the transition from plane-stress to plane-strain is not only a function of W/t, but also of the normalized primary bending radius R_x/t (as reflected in the combined parameter β). Experimental results showed such a transition with one silicon specimen bent to various radii (Kaldor and Noyan, 2002a,b).

The effect of anticlastic curvature on stress state can be realized as follows. When the anticlastic surface can freely develop ($\beta \ll 1$), it has a constant curvature of $\hat{\rho}_y = -\frac{\nu}{R_x}$ by the elastic Poisson's effect. When considering the width effect as β increases, the anticlastic deflection is suppressed in the central area of the plate. As a result, the transverse curvature varies throughout the width, as can be evaluated from Ashwell's closed-form solution (Eq. (5)):

$$\rho_y = \frac{\mathrm{d}^2\tilde{z}}{\mathrm{d}y^2} = -\frac{2\nu}{R_x}[K_2 \cosh \gamma y \cos \gamma y - K_1 \sinh \gamma y \sin \gamma y] \tag{13}$$

Through Poisson's ratio, the restrained anticlastic curvature will affect the principal one. Eq. (12) can be generalized to incorporate the change of the principal bending curvature caused by the anticlastic deformation (for the same bending moment), in terms of a dimensionless parameter ϕ:

$$\rho_x = \frac{1}{R_x} = \frac{M}{EI}(1 - \phi\nu^2) \tag{14}$$

Plane-stress and plane-strain are two special cases corresponding to $\phi = 0$ and $\phi = 1$, respectively. Parameter ϕ has been called the *anticlastic factor* (Pomeroy, 1970). It depends only on β and Poisson's constant ν:

$$\phi = 1 - \frac{2}{k\sqrt{\beta}}\left[\frac{\cosh k\sqrt{\beta} - \cos k\sqrt{\beta}}{\sinh k\sqrt{\beta} + \sin k\sqrt{\beta}}\right] \tag{15}$$

where $k = \sqrt[4]{3(1-\nu^2)}$.

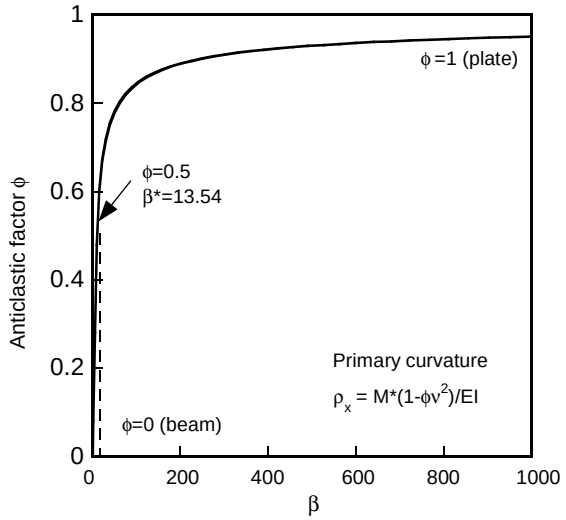

Fig. 8. The variation of the anticlastic factor ϕ with Searle's parameter β.

Fig. 8 shows that ϕ is close to zero when β is small, but that it approaches 1 asymptotically for large β. Eq. (13) reduces to $\frac{d^2\tilde{z}}{dy^2} = -\frac{v}{R_x}$, as $\gamma \to 0$, i.e., the transverse curvature is constant along the width direction, and it has a sign opposite to the primary one. The ratio between these two curvatures is equal to Poisson's ratio, v.

4.3. Application to straightening of an initially curved plate

The foregoing model applies to the initial bending stage of the draw-bend test as an initially flat sheet is drawn over the tool radius. The second stage to be considered is the unbending, or straightening, of the primary curvature as the strip leaves contact with the tooling. Considering the contact constraints with the adjacent tooling, the initial condition of the plate for this stage can be idealized as $R_x^0 = R$ and $R_y^0 = \infty$ (i.e., no anticlastic curvature while in contact with the tool), as shown schematically in Fig. 9. This starting condition is consistent with FE analysis of the draw-bend operation, which shows essentially no transverse curvature near the tool contact.

The curved plate is straightened by applying a uniform moment m_x (per unit width) along the transverse edge, until the primary curvature disappears, Fig. 9. In order to solve the homogeneous ODE (Eq. (4)) in closed-form, the initial plate profile is approximated by a parabolic function, as given by Eqs. (2) and (3). To calculate the shape of a cross-section A–A, $\tilde{z}(y)$, after unbending, the following approximations are utilized:

$$\sinh x \approx \sin x \approx x \quad \text{and} \quad \cosh x \approx \cos x \approx 1 \qquad \text{as } x \to 0 \tag{16}$$

Then, constants K_1 and K_2 in Eq. (6) become

$$K_{1,2} = \frac{\frac{\gamma W}{2} \mp \frac{\gamma W}{2}}{\gamma W + \gamma W} = 0, \frac{1}{2} \tag{17}$$

and the anticlastic deflection reduces to

$$\frac{z}{t} = \frac{v y^2}{2 R_{x0} t} \quad \text{and} \quad \left(\frac{z}{t}\right)_{\max} = \frac{v}{8}\frac{W^2}{R_{x0} t} = \frac{v}{8}\beta_{x0} \tag{18}$$

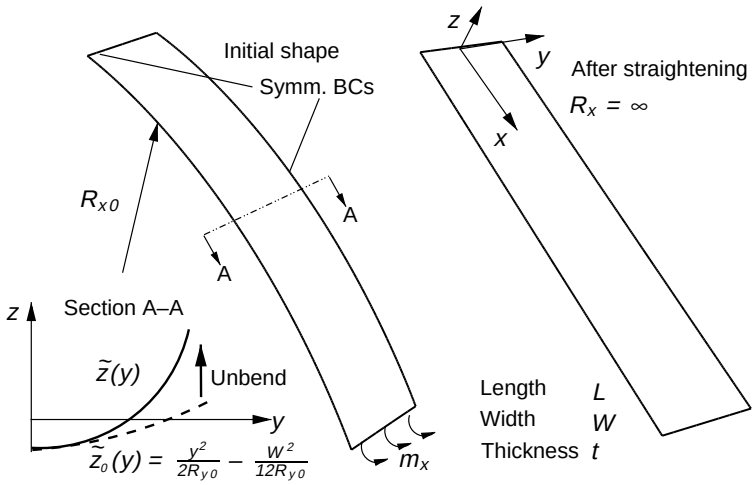

Fig. 9. Unbending (straightening) an initially curved plate.

According to this analysis, straightening an initially curved plate ($\frac{1}{R_{x0}} \neq 0, \frac{1}{R_{y0}} = 0$) can produce large anticlastic deflection. The maximum anticlastic displacement is proportional to Searle's parameter, $\beta_{x0} = \frac{W^2}{R_{x0}t}$, and Poisson's ratio, v. For a typical draw-bend test ($W = 50\,\text{mm}$, $t = 0.9\,\text{mm}$ and $R_{x0} = 3.2\,\text{mm}$), the final anticlastic displacement is up to 30 times the sheet thickness.

To validate the closed-form solution, the straightening problem was FE simulated, using both elastic and elasto-plastic material models. For the latter case, the von Mises yield function and isotropic hardening were used, with a Voce type of hardening law (Wagoner and Chenot, 1997): $\sigma = 381 - 215e^{-9.6\varepsilon}$ (MPa). The FE model is schematically shown in Fig. 9, where a cylindrical plate is flattened by a uniform moment m_x at its transverse edge. Ten 3D shell elements (S4R) were used in the sheet width direction, and a minimum of 40 shell elements in the longitudinal direction so that the turning angle is limited to 2.3° per node. Fifty-one integration points were used through the sheet thickness. These parameters have been shown to be sufficient for accuracy (Li et al., 2002).

The cross-sections at $x = 0$ after unbending are compared with the theoretical solution given by Eq. (18), Fig. 10. As will be discussed, the error caused by parabolic approximation for a circular cross-section is minimal as $x \to 0$. As shown in Fig. 10(a), elastic simulation results agree with the closed-form solution. The maximum anticlastic deflection, $\left(\frac{z}{t}\right)_{\max}$, is invariant for fixed β, regardless of the specimen widths ($W = 5$–$100\,\text{mm}$) and initial radii ($R_{x0} = 5$–$2000\,\text{mm}$). Both simulation and the closed-form solution demonstrate that the maximum anticlastic deflection at plate edges can be several times the plate thickness, while bending an initially flat plate can only produce $z_{\max} = 0.102t$ for $v = \frac{1}{3}$. This difference illustrates why significant anticlastic displacement occurs in the forming step of the draw-bend test, where a sheet is straightened as it slides over a tool surface.

For elasto-plastic material, simulation results deviate from the elastic solution when $\beta > 20$, Fig. 10(b). This is because shear stress is required to maintain compatibility between the elastic ($v = \frac{1}{3}$) and plastic ($v = 0.5$) regions of a plastically bent plate, while that shear effect is neglected in deriving the closed-form solution (Ashwell, 1950). At the same β value, larger deviations exist for narrower plates, because the primary bending radius is smaller and more plastic deformation occurs throughout the plate thickness.

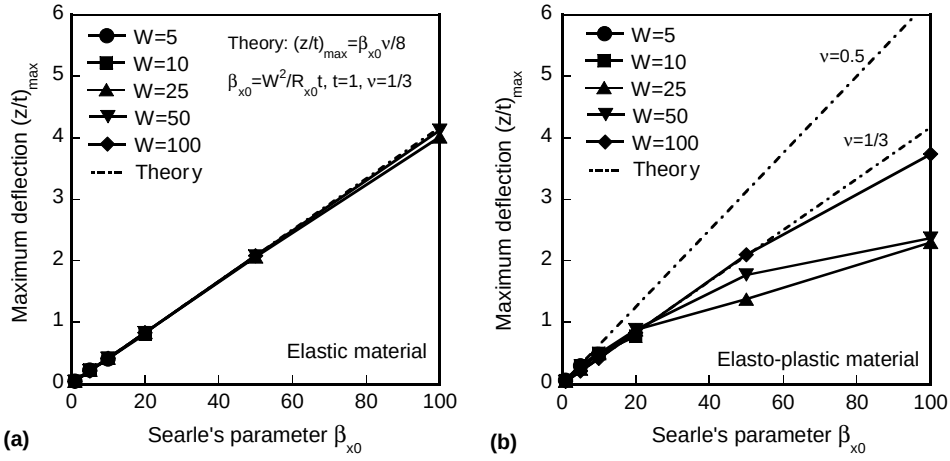

Fig. 10. Simulated maximum anticlastic deflection after unbending for (a) elastic material, and (b) elasto-plastic material.

4.4. Error analysis

As previously mentioned, one major assumption was made in order to solve the fourth order ODE of the elastic bending problem. That is, the initial cross-sections in longitudinal and width directions, and the distorted cross-section in the longitudinal direction, were all approximated by parabola. Or equivalently, curvature is calculated by $\rho = z''$ instead of $\rho = \frac{z''}{(1+z'^2)^{3/2}}$. As shown schematically in Fig. 11, the parabolic approximation causes significant error when the chord length, b, is a significant fraction of the radius of a circle, R. The depth of the parabola $\overline{\mathrm{COD}}$, Δh, and the depth of the arc $\overline{\mathrm{AOB}}$, $\Delta\bar{h}$, both evaluated at $x = \pm\frac{b}{2}$, are calculated by

$$\Delta h = \frac{b^2}{2R} \tag{19}$$

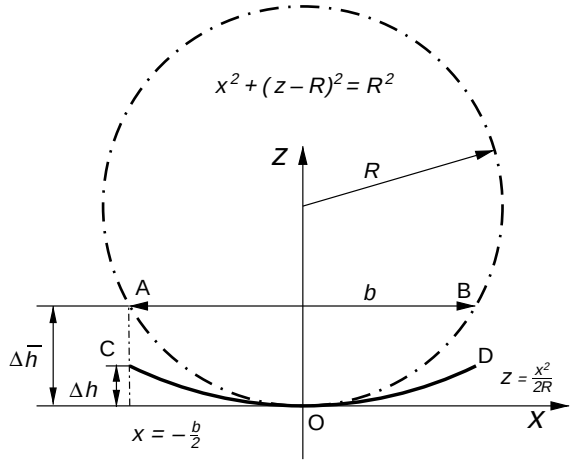

Fig. 11. Error analysis for using parabolic function.

Table 2
Error introduced by using the parabolic function

$\frac{b}{R}$	0.2	0.28	0.45	0.63	1.0	2.0
Err (%)	1	2	5	10	25	100

$$\Delta\bar{h} = R\left[1 - \sqrt{1 - \left(\frac{b}{2R}\right)^2}\right] \tag{20}$$

Applying Taylor's series expansion to the second equation obtains

$$\Delta\bar{h} = \frac{b^2}{8R} + \frac{R}{8}\left(\frac{b}{2R}\right)^4 + \mathcal{O}\left(\frac{b}{2R}\right) \tag{21}$$

where $\mathcal{O}(\cdot)$ indicates the higher order terms. The percentage error introduced by the parabolic function is defined as $\text{Err} = \frac{\Delta\bar{h}-\Delta h}{\Delta h} \times 100\%$. For various ratios of $\frac{b}{R}$, the computed errors are listed in Table 2.

As can be seen from Table 2, the error quickly grows as $\frac{b}{R}$ increases. For the draw-bend test, the unbending takes place from an initially circular strip that was wrapped around a tool of radius R, so that $\frac{b}{R} = 2$. Therefore, large errors in the form of the specimen are expected if the closed-form solution is applied to a cross-section that is located near the plate edges ($x = \frac{L}{2}$, Fig. 9).

5. Experimental results

Two groups of rectangular 6022-T4 aluminum strips, with 0.9 mm thickness, were tested in the current work. Specimens from the first group were 50 mm wide, and were tested under various sheet tensions for two tool radii of 12.7 and 3.2 mm. The purpose was to delineate the region of rapid springback angle change (and concomitant growth of anticlastic curvature). The second group had a strip width ranging from 12 to 50 mm, and was tested using a 12.7 mm tool at two values of normalized sheet tension: $F_b = 0.5$ and 0.9.

5.1. Effect of back force

As shown in Fig. 12, the springback angle decreases with back force, while the anticlastic curvature [1] varies oppositely. As back force approaches 0.7–0.8, there is a dramatic drop in springback angle, accompanied by a rapid increase in anticlastic curvature. The sudden decrease of $\Delta\theta$ has been attributed to the *persistent anticlastic curvature*, which substantially increases the section moment of inertia when $F_b \geqslant 0.7$ (Carden et al., 2002).

Simulated springback angles agree with experiments for both bending radii ($R/t = 3.5$ and $R = 14$), Fig. 12(a). A small bending radius causes more springback, contrary to simple bending results. However, it is in accord with other stretch-bending experiments (Takahashi et al., 1996).

Both experiment and FEM simulation have shown the decrease of anticlastic curvature when $F_b \geqslant 0.9$–1.0, as can be seen in Fig. 12(b). However, simulation results for a small bending radius ($R/t = 3.5$) show an appreciable deviation from measurement. This is presumably because of the use of shell elements which are not accurate for small radius bending (Li et al., 2002). When $R/t < 5$, the general shell assumptions, namely

[1] Measured anticlastic curvature is derived from measured displacement at the center of the arc relative to the edge using Eq. (1). More precision is difficult and unnecessary for small deflections observed.

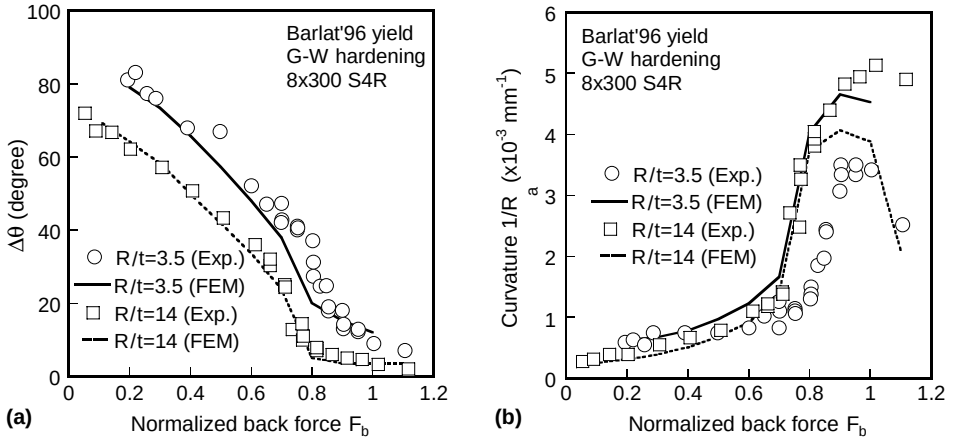

Fig. 12. Effect of back force on (a) springback angle and (b) unloaded anticlastic curvature. Lines are FEM simulation results and markers are experimental data.

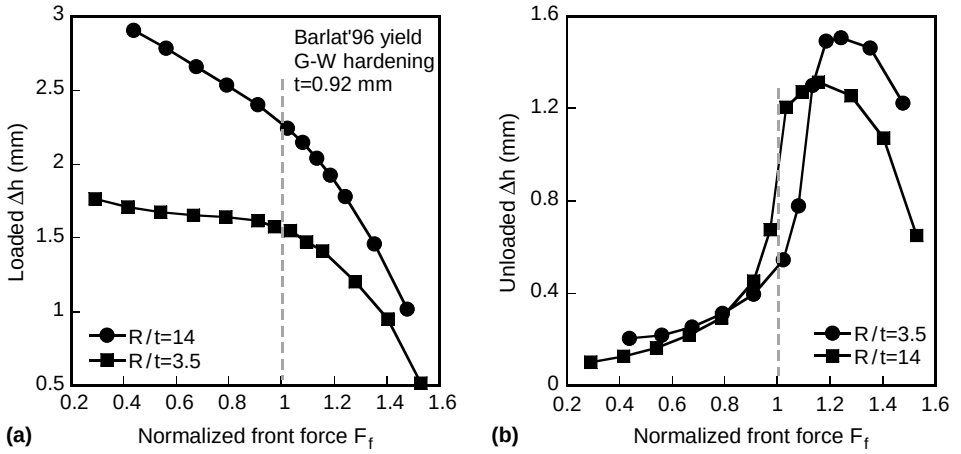

Fig. 13. Variation of maximum anticlastic deflection with front force in the draw-bend test: (a) loaded and (b) unloaded.

zero through-thickness stress and plane section remaining planar after deformation, are no longer valid (Hill, 1950).

The maximum anticlastic deflection (i.e., Δh) from FE simulation is plotted against the normalized front force (F_f), Fig. 13. Before unloading, the maximum anticlastic deflection decreases with increasing front force, and it can be as much as 3 times the sheet thickness when $F_f < 0.5$. After springback, the remaining depth gradually increases with increasing front force, with an abrupt change as the front force approaches unity, Fig. 13(b). This indicates that the persistence of anticlastic curvature is determined by the sheet tension. [2]

Persistent anticlastic curvature has a significant role in reducing springback. As shown in Fig. 14, the bending moment continuously decreases with the back force, as would the springback angle assuming a

[2] A normalized front force of 1 corresponds to a normalized back force of between 0.7 and 0.8 for the draw-bend test of interest.

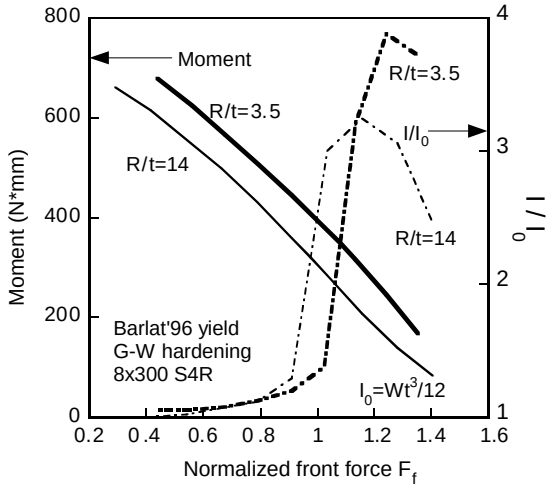

Fig. 14. Moment and normalized section moment of inertia from simulation.

constant moment of inertia of the sheet cross-section. However, the principal bending rigidity of the strip dramatically increases because of the persistent anticlastic curvature during springback when $F_f \geqslant 1.0$. The moment of inertia for a circular cross-section, I, can be calculated using standard formulas (Young, 1989). As illustrated in Fig. 14, the normalized moment of inertia, I/I_0, is increased by a factor of about 3 when the front force exceeds yielding. Here, $I_0 = \frac{Wt^3}{12}$ is the reference moment of inertia for the initial, flat rectangular cross-section. Because of the sudden increase of bending rigidity, springback angle is greatly reduced, Fig. 12(a).

5.2. Effect of specimen width

The experimental results for specimens with various width from 12 to 50 mm are plotted in Fig. 15. For both $F_b = 0.5$ and $F_b = 0.9$, the anticlastic curvature decreases with sample width. However, the springback angle, $\Delta\theta$, first decreases with sample width for the case of $F_b = 0.5$, then it increases after a local minimum

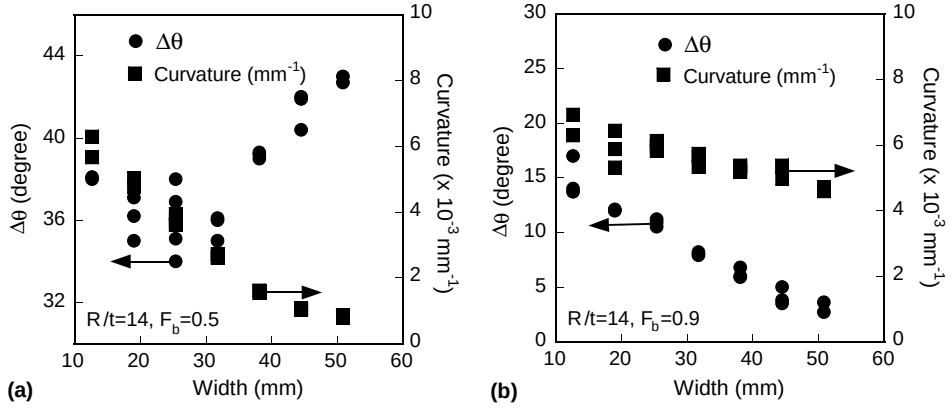

Fig. 15. Springback angle and anticlastic curvature from the draw-bend test for (a) $F_b = 0.5$ and (b) $F_b = 0.9$.

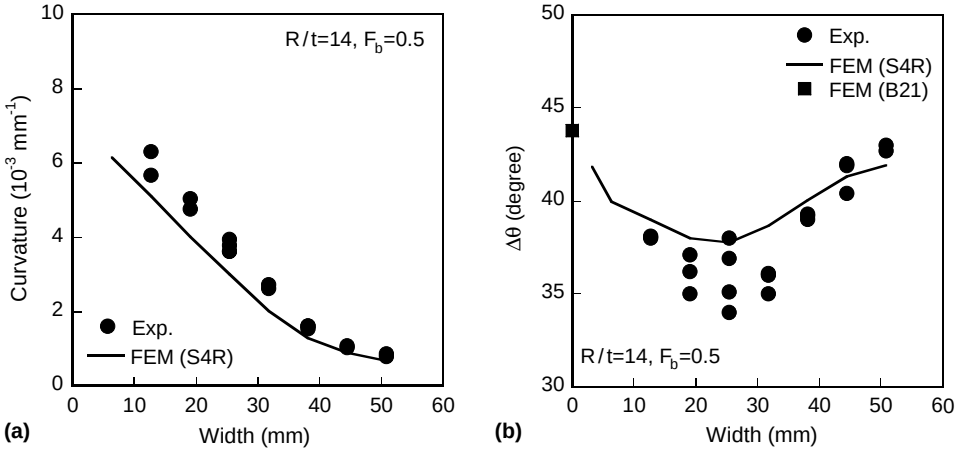

Fig. 16. Comparison of springback results from simulation and measurement for $F_b = 0.5$: (a) springback angle and (b) anticlastic curvature.

that happens around $W = 25$ mm, Fig. 15(a). For $F_b = 0.9$, $\Delta\theta$ monotonically declines with the specimen width, Fig. 15(b).

Finite element simulations were carried out for samples tested with $F_b = 0.5$. As shown in Fig. 16, simulation agrees well with measured springback angle and anticlastic curvature. A 2D simulation result using beam elements is also presented in Fig. 16(a) for comparison. Since a plane-stress state is assumed in the sheet width direction when the beam element (B21) is used, a higher springback angle is attained. For narrower specimens, the value of $\Delta\theta$ from 3D shell element simulations approaches the beam result.

5.3. Application of the elastic bending theory

To make use of the closed-form solution for interpreting these results, the draw-bend test procedure is divided into three sequential steps: bending, unbending and springback. The first step is trivial, in which the sheet is wrapped around the tool under superimposed tension. It is treated as a plane-strain problem, because the strip conforms to the tool surface, and hence transverse displacement can be neglected.

The second and third steps are more complicated 3D problems, because anticlastic deformation is present in both steps. In the unbending step, the strip loses its primary curvature ($\frac{1}{R}$, when it is in contact with the tool) as it slides over the tool surface. Eventually, it becomes straight in the longitudinal direction, i.e., $R_x^{(2)} = \infty$. Meanwhile, a transverse curvature, $\frac{1}{R_x^{(2)}}$, is developed in the sheet width direction. In the last step, the sample attains a primary curvature in the *side-wall curl* region after springback. The radius of this curvature, r', depends on sheet tension, tool radius and friction condition, as well as material properties such as yield surface shape and strain hardening law (Carden et al., 2002; Li et al., 2002). During springback, the previously developed anticlastic curvature will change from $\frac{1}{R_y^{(2)}}$ to $\frac{1}{R_a}$. Table 3 summarizes the primary and anticlastic curvatures involved in the three steps.

Table 3
The radii of primary and anticlastic curvature in the draw-bend test

Step	R_{x0}	R_{y0}	R_x	R_y
1 Bending	∞	∞	R	∞
2 Unbending	R	∞	∞	$R_y^{(2)}$
3 Springback	∞	$R_y^{(2)}$	r'	R_a

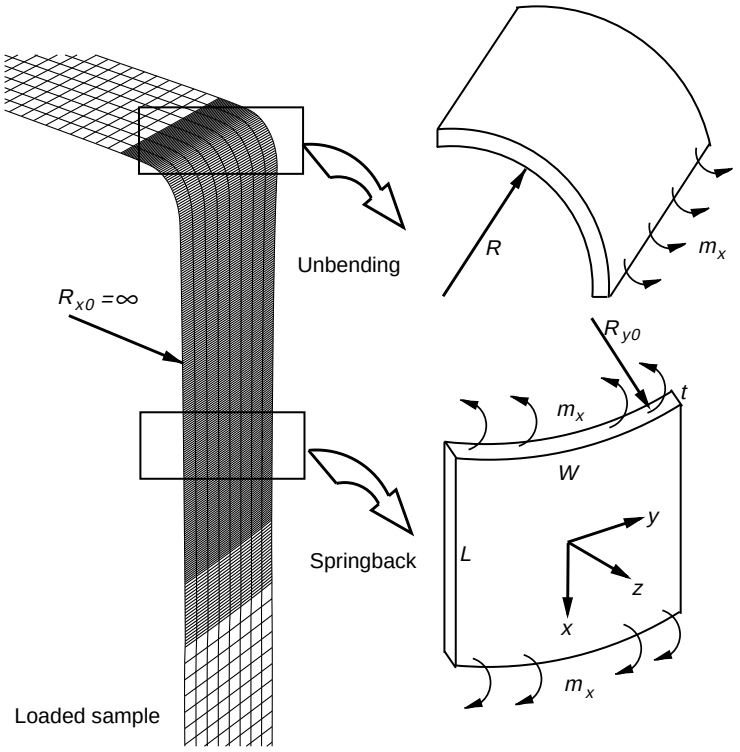

Fig. 17. Unbending and springback analysis for draw-bend test.

The elastic theory of plate bending can be applied to the last two steps, as schematically shown in Fig. 17. Apparently, the unbending process (Step 2) involves plasticity, and thus elastic plate theory will not give satisfactory results. As discussed in Section 4.3, the elastic theory overpredicts the maximum anticlastic deflection by a factor of 10 for a typical draw-bend test ($R/t = 3.5$).

Nonetheless, it helps to understand why the maximum anticlastic deflection before unloading can be as much as 3 times the sheet thickness in the draw-bend test. For the last step, the application of elastic theory is reasonable, since springback is usually dominated by elastic deformation. The outputs of the unbending step from FE simulation, i.e., the transverse and longitudinal cross-section shapes, are used as input for the analysis in the springback step. Then, the predictions by the closed-form solution are compared with the FE results; and, for two cases, with experimental data as well. The goal is to explain why anticlastic curvature persists after springback only for large sheet tensions.

To apply the elastic theory for the springback analysis, three radii of curvature, $R_x^{(2)}$, $R_y^{(2)}$ and $R_x^{(3)}$ from FE simulation, are used as input to the closed-form solution, in order to calculate the anticlastic curvature after springback, $R_y^{(3)}$. The predicted maximum anticlastic deflection is then compared with FE results. As shown in Fig. 18, the elastic theory prediction agrees qualitatively with the finite element simulations for both tool radii, but it under-estimates the magnitude of anticlastic deflection. Both FE simulations and elastic predictions show that the unloaded depth of the anticlastic profile initially increases with sheet tension, but decreases after front force exceeds the yielding force of the strip, which corresponds to the occurrence of the persistent anticlastic curvature after springback. It is also noted that elastic prediction deviates more from FE results as normalized front force is larger than unity. On the other hand, the elastic solution is closer to the finite element simulation for a larger tool radius. One possible explanation is that springback

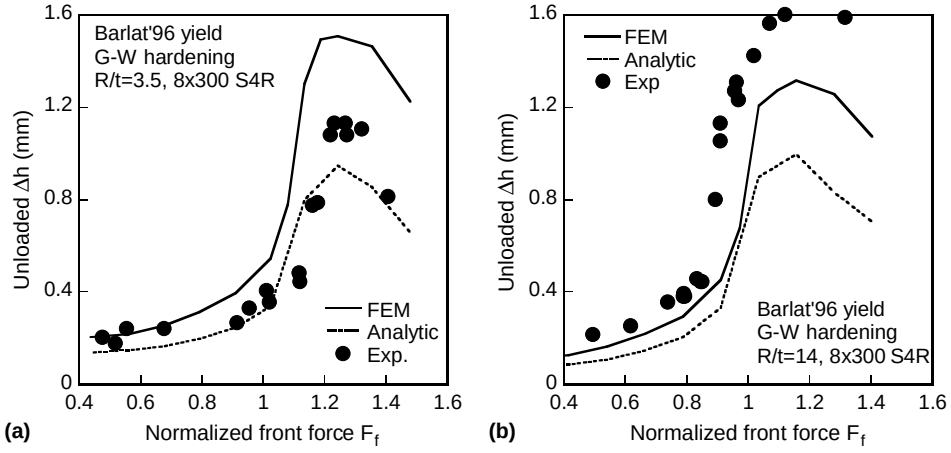

Fig. 18. Comparison of simulated and analytically predicted maximum anticlastic deflections for draw-bend tested samples after springback: (a) $R/t = 3.5$ and (b) $R/t = 14.0$.

also involves plastic deformation because of the reduction of flow stress after a reversed strain path (Geng and Wagoner, 2002). Previous work showed that plasticity during springback can significantly change the residual stress distribution, and a purely elastic unloading scheme causes a difference of 10° of springback angle (Li et al., 2002).

The calculated cross-section profiles are compared in Fig. 18 with FE simulations and experimental data, for two specimens tested at $F_b = 0.4$ and 0.8, with $R/t = 14.0$, Fig. 19. For small back force, the anticlastic deflection is localized toward the specimen edges, while the cross-section is nearly circular for $F_b = 0.8$. The overall agreement between elastic prediction, finite element simulation and experimental measurement is

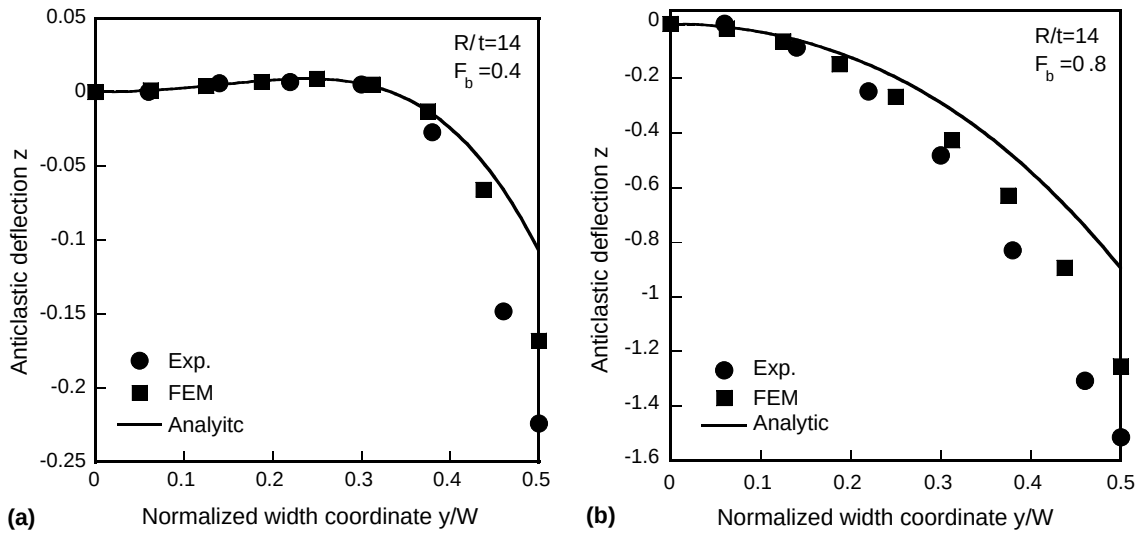

Fig. 19. Comparison of measured, simulated and analytically predicted anticlastic profiles for draw-bend tested samples: (a) $F_b = 0.4$ and (b) $F_b = 0.8$.

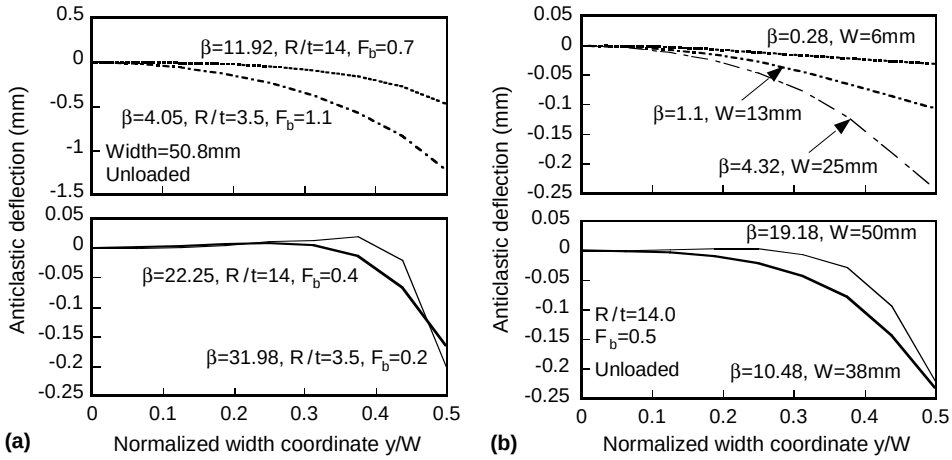

Fig. 20. Effect of Searle's parameter β on the cross-section shape: (a) for various back forces and (b) for specimens with different widths.

satisfactory. However, the elastic solution tends to under-estimate the magnitude of anticlastic deflection, as previously demonstrated by Fig. 18.

6. Discussion

Based on the previous analysis, the shape of the anticlastic surface of a draw-bend tested sample can be characterized by a dimensionless parameter, β, which combines the influence of tool radius, sheet tension (via the curl radius r') and sample geometry (W/t). This can be emphasized by the anticlastic profiles

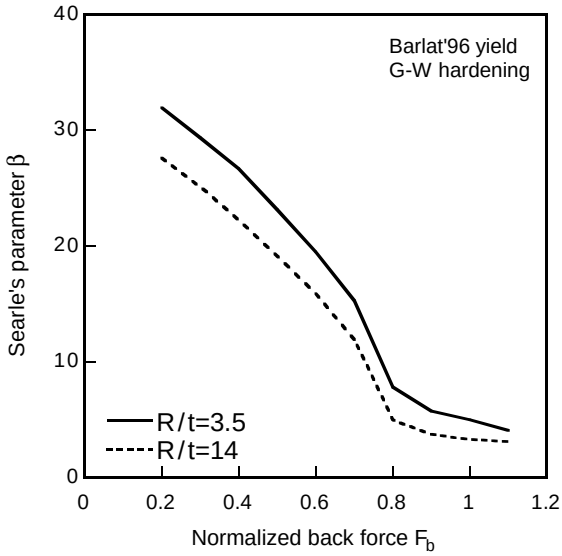

Fig. 21. Variation of Searle's parameter β with back force.

computed by FE simulation, Fig. 20. Specimens from the first test group have the same width, but sheet tension and bending radius are different, Fig. 20(a). Fig. 20(b) shows the cross-section profiles of samples with various widths ranging from 12 to 50 mm tested with the $R/t = 14$ tool. Both cases demonstrate that β uniquely determines the shape of the anticlastic surface. When $\beta < 10$–15, all cross-sections are nearly circular. As β increases, anticlastic deflection tends to localize toward the sheet edges, while the sheet central area is essentially flat.

As a final note, it appears that the variation of β with respect to the back force is similar to that of $\Delta\theta$, Fig. 21. In addition to the steady decrease with F_b, β rapidly decreases around $F_b = 0.7$–0.8. This closely matches the sudden decrease of $\Delta\theta$ in Fig. 12(a), as well as the sudden increase of the anticlastic curvature in Fig. 12(b). Therefore, it is clear that the *persistent anticlastic curvature* is determined by the interplay between specimen geometry, back force and tool radius, as reflected by Searle's parameter β.

7. Conclusions

Elastic bending theory, finite element simulation, and draw-bend experiments have been utilized to investigate the role of forming variables on anticlastic curvature. The following conclusions were reached:

1. Springback steadily decreases as sheet tension increases, with sudden decline of springback angle as the front pulling force approaches yielding. *Persistent anticlastic curvature* is identified as the cause of this rapid change. Larger tool radius leads to less springback, but has a less significant effect than sheet tension.
2. In the draw-bend test, anticlastic curvature is developed in the unbending process during forming, and it persists after springback when the applied sheet tension exceeds a critical value near yield. The persistent anticlastic curvature significantly increases the section moment of inertia, and thus dramatically reduces springback.
3. For $F_b = 0.5$ and $R/t = 14$, the springback angle first decreases, then increases with the strip width, but the anticlastic curvature monotonically decreases with the specimen width. However, both springback angle and anticlastic curvature decrease with the specimen width for $F_b = 0.9$.
4. The occurrence and persistence of anticlastic curvature in the draw-bend test can be understood through the use of the elastic bending theory. The cross-section shape after unloading is determined by Searle's parameter, β, which depends on the specimen geometry (W/t) and sheet tension (via the curl radius R_x). The rapid decrease in springback angle at $F_b = 0.7$–0.8 corresponds to a critical β value of 10–15, above which the anticlastic displacement tends to concentrate toward the sheet edges.
5. The stress state in the lateral direction (plane-stress or plane-strain) cannot be simply identified by the sheet width-to-thickness ratio, even for simple bending problems. The radius of primary bending curvature can affect deformation mode too, via Searle's parameter. For the draw-bend test, the springback process is closer to plane-stress rather than plane-strain, because of the *persistent anticlastic curvature*.

Acknowledgments

We would like to thank the National Science Foundation (DMR 0139045) and the Center for Advanced Materials and Manufacturing of Automotive Components (CAMMAC) at The Ohio State University for funding support. Computer simulations were conducted with the support of the Ohio Supercomputer Center (PAS0080).

References

Abaqus, 2001. Abaqus/Standard User's Manual 6.2. Pawtucket, RI 02860.

Ashwell, D., 1950. The anticlastic curvature of rectangular beams and plates. Journal of Royal Aeronautical Society 54, 708–715.

Ashwell, D., 1952. A characteristic type of instability in the large deflections of elastic plates. Proceedings of Royal Society of London A 214, 98–118.

Ashwell, D., Greenwood, E., 1950a. The pure bending of rectangular plates. Engineering (July), 51–53.

Ashwell, D., Greenwood, E., 1950b. The pure bending of rectangular plates. Engineering (July), 76–78.

Barlat, F., Maeda, Y., Chung, K., Yanagawa, M., Brem, J., Hayashida, Y., Lege, D., Matsui, K., Murtha, S., Hattori, S., Becker, R., Makosey, S., 1997. Yield function development for aluminum alloy sheet. Journal of Mechanics and Physics of Solids 45 (11/12), 1727–1763.

Bellow, D., Ford, G., Kennedy, J., 1965. Anticlastic behavior of flat plates. Experimental Mechanics 5 (7), 227–232.

Carden, W., Geng, L., Matlock, D., Wagoner, R., 2002. Measurement of springback. International Journal of Mechanical Sciences 44 (1), 79–101.

Conway, H., Farnham, K., 1965. Anticlastic curvature of strips of variable thickness. International Journal of Mechanical Science 7 (2), 451–458.

Conway, H., Nickola, W., 1965. Anticlastic action of flat sheets in bending. Experimental Mechanics 5 (1), 115–119.

Davies, R., 1984. Sidewall curl in high-strength steels. Journal of Applied Metalworking 3 (2), 120–126.

Fung, Y., Wittrick, W., 1954. The anticlastic curvature of a strip with lateral thickness variation. Journal of Applied Mechanics 21, 351–358.

Fung, Y., Wittrick, W., 1955. A boundary layer phenomenon in the large deflection of thin plates. The Quarterly Journal of Mechanics and Applied Mathematics 8 (2), 191–210.

Geng, L., Wagoner, R., 2002. Role of plastic anisotropy and its evolution on springback. International Journal of Mechanical Sciences 44 (1), 123–148.

Gerard, G., 1946. Effect of bend width upon minimum bend radii. Journal of the Aeronautical Sciences 14, 161–170.

Hill, R., 1950. The Mathematical Theory of Plasticity. Clarendon Press, Oxford.

Horrocks, D., Johnson, W., 1967. On anticlastic curvature with special reference to plastic bending: A literature survey and some experimental investigations. International Journal of Mechanical Science 9, 835–861.

Kaldor, S., Noyan, I., 2002a. Differentiating between elastically bent rectangular beams and plates. Applied Physics Letters 80 (13), 2284–2286.

Kaldor, S., Noyan, I., 2002b. Erratum: "differentiating between elastically bent rectangular beams and plates". Applied Physics Letters 80 (25), 2286–4871.

Lamb, H., 1891. On the flexure of a flat elastic spring. Philosophical Magazine 31, 182–195.

Li, K., Carden, W., Wagoner, R., 2002. Simulation of springback. International Journal of Mechanical Sciences 44 (1), 103–122.

Marciniak, Z., Duncan, J., 1992. The Mechanics of Sheet Metal Forming. Edward Arnold, London.

Marguerre, K., 1938. Zur theore der gekrümmten platte grosser formänderung. In: Den Hartog, J., Peters, H. (Eds.), Proceedings of the 5th International Congress for Applied Mechanics. John Wiley, New York, pp. 93–101.

Parco Prelube MP 404, 2001. Manufactured and distributed by Parker Amchem, Henkel Surface Technologies Corporation. 32100 Stephenson Highway, Madison Heights, MI 48071.

Pao, Y., Conway, H., 1966. An optimum study of the anticlastic deformations of strips with tapered edges. International Journal of Mechanical Science 8 (1), 65–76.

Pomeroy, R., 1970. The effect of anticlastic bending on the curvature of beams. International Journal of Solids and Structures 6, 277–285.

Searle, G., 1908. Experimental Elasticity: A Manual for the Laboratory. Cambridge University Press, Cambridge.

Takahashi, S., Kuwabara, T., Ito, K., 1996. Springback analysis of sheet metal subjected to bending-unbending under tension—Part II (experimental verification). In: Altan, T. (Ed.), Advanced Technology of Plasticity—Proceedings of the 5th ICTP, vol. 2, Columbus, OH, pp. 747–750.

Vallance, D., Matlock, D., 1992. Application of the bending-under-tension friction test to coated sheet steels. Journal of Materials Engineering and Performance 1, 685–694.

von Kármán, T., 1910. Festigkeitsprobleme im maschinenbau. Encyklopädie der Mathematischen Wissenschaften 4 (4), 311–385.

Wagoner, R., Chenot, J.-L., 1997. Fundamentals of Metal Forming. John Wiley, New York.

Wang, J.F., Wagoner, R., Carden, W.D., Matlock, D., Barlat, F., 2004. Creep and an elasticity in the springback of aluminum. International Journal of Plasticity 20 (12), 2209–2232.

Wenzloff, G., Hylton, T., Matlock, D., 1992. Technical note: a new test procedure for the bending under tension friction test. Journal of Materials Engineering and Performance 1, 609–614.

Young, W., 1989. Roark's Formulas for Stress and Strain, sixth ed. McGraw-Hill, New York (Table I, Case 20).

Yu, T., Zhang, L., 1996. Plastic Bending, Theory and Applications. World Scientific, Singapore.